

One-Component Order Parameter in URu₂Si₂ Uncovered by Resonant Ultrasound Spectroscopy and Machine Learning

Sayak Ghosh,^{1†} Michael Matty,^{1†} Ryan Baumbach,² Eric D. Bauer,³
K. A. Modic,⁴ Arkady Shekhter,² J. A. Mydosh,⁵
Eun-Ah Kim¹ and B. J. Ramshaw^{1*}

¹Laboratory of Atomic and Solid State Physics,
Cornell University, Ithaca, NY, 14853

²National High Magnetic Field Laboratory,
Florida State University, Tallahassee, FL 32310, USA

³Los Alamos National Laboratory, Los Alamos, NM, USA 87545.

⁴Max-Planck-Institute for Chemical Physics of Solids, Dresden, Germany 01187.

⁵Kamerlingh Onnes Laboratory and Institute Lorentz,
Leiden University, 2300 RA Leiden, The Netherlands.

† Authors contributed equally to this work.

*To whom correspondence should be addressed: bradramshaw@cornell.edu.

The unusual correlated state that emerges in URu₂Si₂ below $T_{\text{HO}} = 17.5$ K is known as hidden order because even basic characteristics of the order parameter, such as its dimensionality (whether it has one component or two), are “hidden”. We use resonant ultrasound spectroscopy to measure the symmetry-resolved elastic anomalies across T_{HO} . We observe no anomalies in the shear elastic moduli, providing strong thermodynamic evidence for a one-component order parameter. We develop a machine learning framework that reaches this conclusion directly from the raw data, even in a crystal that is too small for

traditional resonant ultrasound. Our result rules out a broad class of theories of hidden order based on two-component order parameters, and constrains the nature of the fluctuations from which unconventional superconductivity emerges at lower temperature. Our machine learning framework is a powerful new tool for classifying the ubiquitous competing orders in correlated electron systems.

Introduction

Phase transitions mark the boundary between different states of matter, such as liquid to solid, or paramagnet to ferromagnet. At the phase transition the system lowers its symmetry: translationally invariant liquids become crystalline solids; paramagnetic spins align to break time reversal and rotation symmetry in a magnet. The conventional description of a second-order phase transition—Landau theory—requires knowledge of which symmetries are broken in the low-temperature phase to construct an order parameter (OP). Several possibilities have been put forth for the symmetry of the OP in the hidden order (HO) state of URu_2Si_2 (Table 1), but most of these rely on specific microscopic mechanisms that are difficult to verify experimentally (1, 2).

The purpose of this paper is to use resonant ultrasound spectroscopy (RUS) to place strict thermodynamic constraints—independent of microscopic mechanism—on the OP symmetry in URu_2Si_2 . While RUS is a powerful technique—capable of constraining or identifying the symmetries broken at a phase transition (3)—it has one significant drawback: a single missing resonance renders an entire spectrum unusable. This is because traditional RUS data analysis relies on solving the elastic wave equation and mapping the computed resonances one-to-one with measured resonances—a single missing resonance invalidates this mapping. Here we develop a new machine-learning based approach. We take advantage of the fact that neural networks

can be trained to recognize features in complex data sets and classify the state of matter that produce such data (4–9). We validate this approach by analyzing an RUS data set that we are confident can also be analyzed using traditional methods (data from a large single-crystal of URu_2Si_2 with a well-defined geometry). We then analyze data from a higher quality URu_2Si_2 sample that has an ill-defined geometry—a task that is impossible for the traditional analysis method, but which is easily performed by our neural network.

While the broken symmetries of HO are unknown, most theories assume some form of ‘multipolar order’, whereby localized $5f$ electrons on the uranium site occupy orbitals that order below $T_{\text{HO}} = 17.5$ K. However, direct experimental evidence for localized $5f$ electrons—such as crystalline electric field level splitting—does not exist (1), leaving room for theories of HO based on itinerant $5f$ electrons. Many possible OPs remain in contention, but, whether itinerant or localized, all theories of HO can be classified based on the dimensionality of their point group representation: one-component (10–19) or two-component (20–26) (see Table 1 and footnote (27)). Theories of two-component OPs are motivated largely by the experiments of Okazaki et al. (28) and Tonegawa et al. (29), which detect a small C_4 symmetry breaking at T_{HO} . More recent X-ray experiments have cast doubt on these results (30), leaving even the dimensionality of the OP in URu_2Si_2 an open question.

Determining OP dimensionality is more than an exercise in accounting: the two-component nature of loop currents allows for dynamics that have been suggested to explain the pseudogap in high- T_c cuprates (31); and the proposed two-component $p_x + ip_y$ superconducting state of Sr_2RuO_4 has a unique topological structure that can support Majorana fermions (32, 33). Establishing the dimensionality of the HO state not only allows us to rigorously exclude a large number of possible OPs, it also provides a starting place for understanding the unusual superconductivity that emerges at lower temperature in URu_2Si_2 .

Dimensionality	Symmetry	Reference
One-component	A_{1g}	Harrison and Jaime (34)
	A_{1u}	Kambe <i>et al.</i> (19)
	A_{2g}	Haule and Kotliar (14), Kusunose and Harima (15), Kung <i>et al.</i> (17)
	A_{2u}	Cricchio <i>et al.</i> (16)
	B_{1g}	Ohkawa and Shimizu (11), Santini and Amoretti (12)
	B_{1u}	Kiss and Fazekas (13)
	B_{2g}	Ohkawa and Shimizu (11), Santini and Amoretti (12), Harima <i>et al.</i> (10)
	B_{2u}	Kiss and Fazekas (13)
Two-component	E_g	Thalmeier and Takimoto (20), Tonegawa <i>et al.</i> (23), Rau and Kee (22), Riggs <i>et al.</i> (26)
	E_u	Hoshino <i>et al.</i> (21), Ikeda <i>et al.</i> (25), Riggs <i>et al.</i> (26)
	$E_{3/2,g}$	Chandra <i>et al.</i> (35)

Table 1: Proposed order parameters of the HO state in URu₂Si₂, classified by their dimensionality and their point-group representation. Note that designations such as “hexadecapole” order are only applicable in free space—crystalline electric fields break these large multipoles into the representations listed in this table.

Experiment

Resonant Ultrasound Spectroscopy of URu₂Si₂

RUS measures the mechanical resonance frequencies of a single-crystal specimen—analogueous to the harmonics of a guitar string but in three dimensions (see Fig. 1a). A subset of this spectrum for a 3 mm x 2.8 mm x 2.6 mm crystal of URu₂Si₂ (sample S1) is shown in Fig. 1b, with each peak occurring at a unique eigenfrequency of the elastic wave equation (see supplementary information). Encoded within these resonances is information about the sample’s dimensions and density, which are known, and the six elastic moduli, which are unknown. As electrons and phonons are coupled strongly in metals, the temperature dependence of the elastic moduli reveals fluctuations and instabilities in the electronic subsystem. In particular, elastic moduli are sensitive to symmetry breaking at electronic phase transitions (3, 36). The difficulty lies in converting the temperature dependence of the resonance spectrum into the temperature dependence of the elastic moduli. The traditional analysis involves solving the 3D elastic wave equation and adjusting the elastic moduli to match the experimental resonance spectrum. However, if even a single resonance is missing from the spectrum (e.g. due to weak coupling of a particular mode

to the transducers), then this analysis scheme breaks down (see Ramshaw *et al.* (3) for further discussion of this problem).

Fig. 1c shows the temperature dependence of seven representative elastic resonances through T_{HO} (29 resonances were measured in total). Note that while some resonances show a step-like discontinuity or ‘jump’ at T_{HO} , others do not. This jump is present in the elastic moduli for all second-order phase transitions (3, 36, 37), but has never before been observed in URu_2Si_2 due to insufficient experimental resolution (38–42). Traditional RUS produces spectra at each temperature, such as the one shown in Fig. 1b, by sweeping the entire frequency range using a lock-in amplifier. The resonance frequencies are then extracted by fitting Lorentzians to each peak (36). We have developed a new approach whereby the entire spectrum is swept only once—to identify the resonances—and then each resonance is tracked as a function of temperature with high-precision using a phase-locked loop. This increases the density of data points per unit temperature by roughly a factor of 1000, and increases the signal to noise by a factor of 30 (see methods).

The complex strain fields produced at each resonance frequency (Fig. 1a) can be broken down locally into irreducible representations of strain (ϵ_k). Each irreducible strain then couples to an OP η of a particular symmetry in a straightforward manner (37). In this way, analysis of the temperature dependence of the resonance frequencies can identify or constrain the OP symmetry. In a tetragonal crystal, such as URu_2Si_2 , elastic strain breaks into five irreducible representations (Fig. 2): two compressive strains transforming as the identity A_{1g} representation, and three shear strains transforming as the B_{1g} , B_{2g} and E_g representations. Allowed terms in the free energy \mathcal{F} are products of strains and OPs that transform as the A_{1g} representation. As HO is thought to break at least translational symmetry, the lowest-order terms allowed by both one-component and two-component OPs are linear in the A_{1g} strains and quadratic in OP: $\mathcal{F} = \epsilon_{A_{1g}} \cdot \eta^2$ (see footnote (43)). Quadratic-in-order-parameter, linear-in-strain coupling

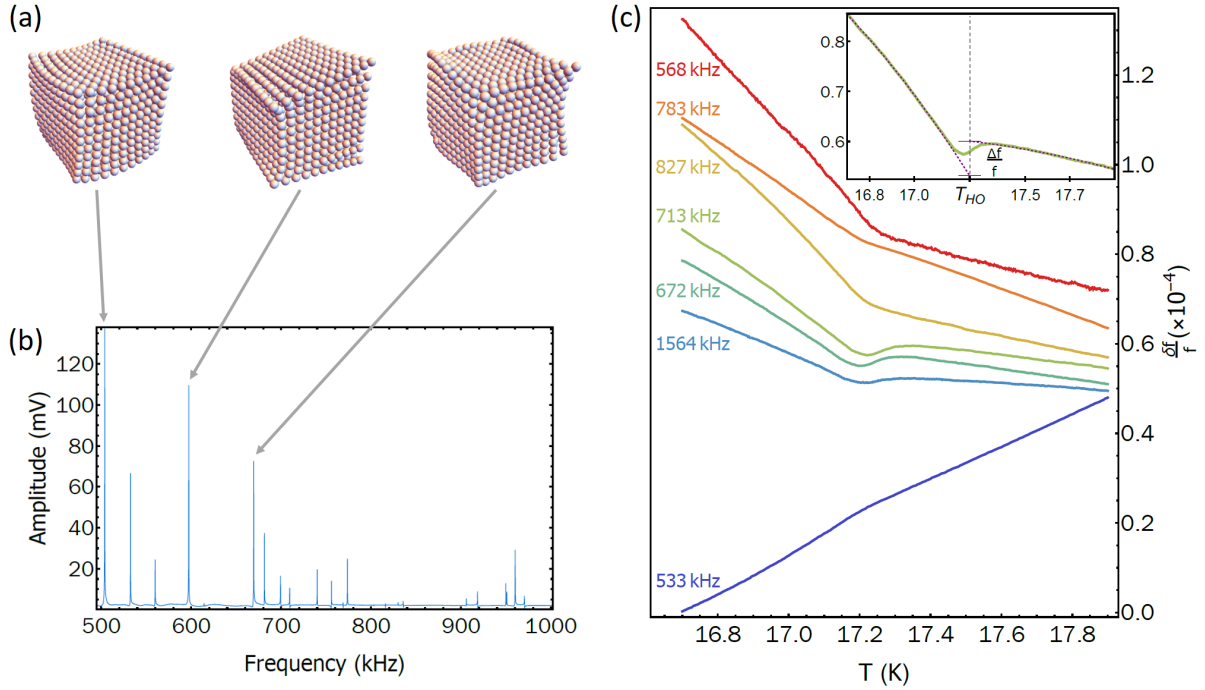


Figure 1: **Resonant ultrasound spectroscopy across T_{HO} in URu_2Si_2 .** (a) Schematic resonance eigenmodes obtained as a solution to the 3D elastic wave equation. Each mode contains a unique proportion of the five irreducible strains (see Fig. 2a). (b) Room temperature ultrasonic spectrum of sample S1, shown between 500 kHz and 1 MHz. (c) Temperature evolution of seven characteristic resonances, out of 29 total measured resonances, near the HO transition—plots are shifted vertically for clarity. Three resonances (672 kHz, 713 kHz and 1564 kHz) show jumps at T_{HO} (inset illustrates what is meant by the jump), while the others do not, signifying contributions from different symmetry channels.

produces a discontinuity in the associated elastic modulus at the phase transition: this jump is related to discontinuities in the specific heat and other thermodynamic quantities through Ehrenfest relations (36, 44). For OPs with one-component representations (any of the A_i or B_i representations of D_{4h}), only the elastic moduli corresponding to A_{1g} compressional strains couple in this manner. In contrast, shear strains couple as $\mathcal{F} = \epsilon_k^2 \cdot \eta^2$ and show at most a change in slope at T_{HO} (3). Thus c_{33} , c_{23} and $(c_{11} + c_{12})/2$ may exhibit jumps at phase transitions corresponding to one-component OPs, while $(c_{11} - c_{12})/2$, c_{66} , and c_{44} cannot.

Two-component OPs (of the E_i representations), on the other hand, have bilinear forms that can couple with two of the shear strains to first order. A two-component OP, $\vec{\eta} = \{\eta_x, \eta_y\}$, has the bilinears $\eta_x^2 + \eta_y^2$, $\eta_x^2 - \eta_y^2$, and $\eta_x \eta_y$; of the A_{1g} , B_{1g} , and B_{2g} representations, respectively. In addition to the standard $\epsilon_{A_{1g}} \cdot \eta_x^2 + \eta_y^2$ terms, the free energy now contains the terms $\epsilon_{B_{1g}} \cdot (\eta_x^2 - \eta_y^2)$ and $\epsilon_{B_{2g}} \cdot \eta_x \eta_y$. A second order phase transition characterized by a two-component OP therefore exhibits discontinuities in the B_{1g} and B_{2g} shear elastic moduli ($(c_{11} - c_{12})/2$ and c_{66} , respectively), in addition to jumps in the compressional A_{1g} moduli (see SI for a discussion of the $E_{3/2,g}$ representation, pertaining to “hastatic” order).

We first perform a traditional RUS analysis, extracting the temperature dependence of the six elastic moduli (Fig. 2b and c) from 29 measured resonances by solving the elastic wave equation and fitting the spectrum using a genetic algorithm (see SI of Ramshaw *et al.* (3) for details). The evolution of the elastic moduli across T_{HO} shows jumps in two of the A_{1g} elastic moduli, whereas the B_{1g} and B_{2g} shear moduli show only a break in slope at T_{HO} to within our experimental uncertainty (Fig. 2d). Jumps in the shear moduli would be expected for any order parameter of the two-component E_i representations (20–26)—the fact that we do not resolve any shear jumps constrains the OP of the HO phase to belong to a one-component representation of D_{4h} . The fact that we do not resolve a jump in c_{33} is consistent with the magnitudes of the jumps in $(c_{11} + c_{12})/2$ and c_{23} —see SI for details.

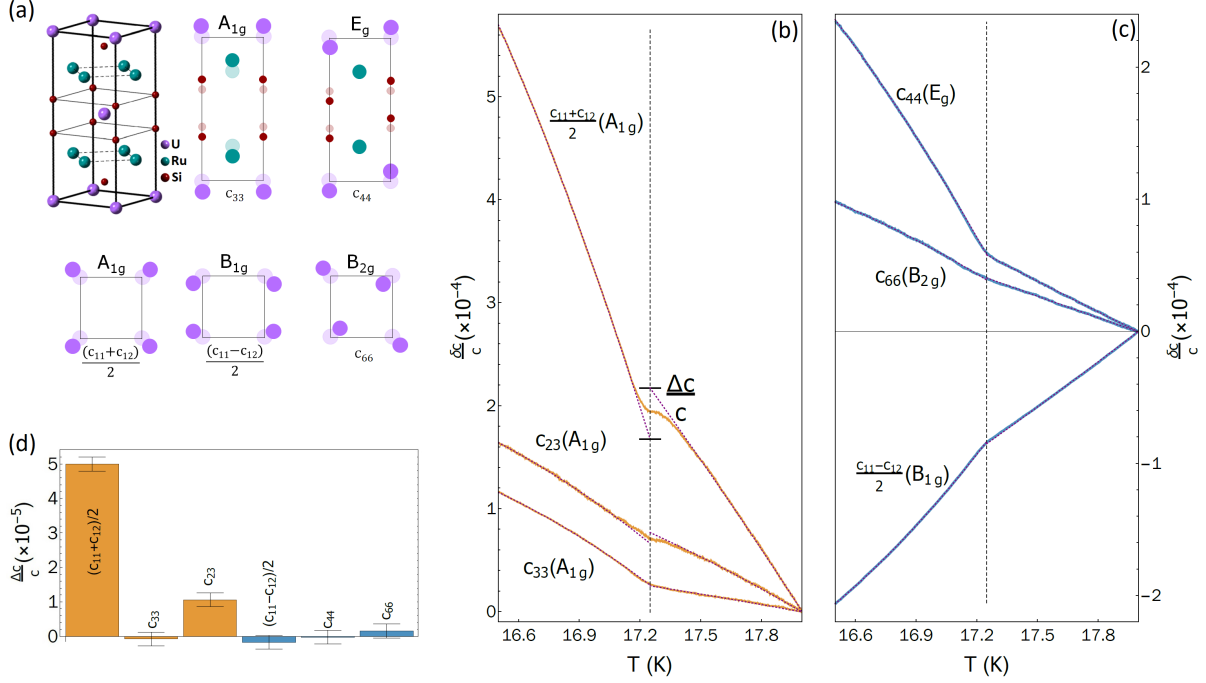


Figure 2: **Traditional extraction of symmetry information from elastic moduli.** (a) The tetragonal crystal structure of URu_2Si_2 and its five irreducible representations of strain, along with the associated moduli. Each resonance shown in Fig. 1a can be decomposed into this basis set of strains, modulated in phase at long wavelengths throughout the crystal. c_{23} characterizes the direct coupling between the two A_{1g} strains. (b) Compressional (A_{1g} , shown in orange) and (c) shear (B_{1g} , B_{2g} , and E_g , shown in blue) elastic moduli, with dashed guides to the eye showing the temperature dependence extrapolated from below and above T_{HO} . The absolute values (in GPa) of the moduli at ~ 20 K were determined to be $(c_{11} + c_{12})/2 = 218.0$, $c_{33} = 307.4$, $c_{23} = 112.8$, $(c_{11} - c_{12})/2 = 65.2$, $c_{66} = 140.6$ and $c_{44} = 101.8$. (d) The magnitude of the jumps at T_{HO} with their experimental uncertainties. A large jump occurs in $(c_{11} + c_{12})/2$ at T_{HO} , along with a small jump in c_{23} . The shear moduli, on the other hand, show only a change in slope at T_{HO} —this constrains the OP of the HO state to transform as a one-component representation.

In principle this traditional analysis is sufficient to determine the order-parameter dimensionality in URu_2Si_2 . The process of solving for the elastic moduli, however, incorporates systematic errors arising from sample alignment, parallelism, dimensional uncertainty, and thermal contraction. Even more detrimental is the possibility that the measured spectrum is missing a resonance, rendering the entire analysis incorrect. While we are confident in our analysis for the particularly large and well-oriented sample S1, large samples of URu_2Si_2 are known to be of slightly lower quality (45). Smaller, higher-quality crystals of URu_2Si_2 do not lend themselves well to RUS studies, being hard to align and polish to high precision. Smaller samples also produce weaker RUS signals, making it easier to miss a resonance. We have therefore developed a new method for extracting symmetry information directly from the resonance spectrum, without needing to first extract the elastic moduli themselves, even if the spectrum is incomplete. This method takes advantage of the power of machine learning algorithms to recognize patterns in complex data sets.

Machine Learning for Resonant Ultrasound Spectroscopy

Artificial neural networks (ANNs) are popular machine learning tools due to their ability to classify objects in highly non-linear ways. In particular, ANNs can approximate smooth functions arbitrarily well (46). Here we train an ANN to learn a function that maps the jumps in ultrasonic resonances at a phase transition to one of two classes, corresponding to either a one-component or two-component OP. one-component OPs induce jumps only in compressional elastic moduli, whereas two-component OPs also induce jumps in two of the shear moduli. Phase transitions with two-component OPs should therefore show jumps in more ultrasonic resonances at a phase transition than phase transitions with one-component OPs. Our intent is that this difference in the distribution of jumps can be learned by an ANN to discriminate between one-component and two-component OPs.

An ANN must be trained with simulated data that encompasses a broad range of possible experimental scenarios. In our case we simulate RUS spectra given assumptions about the sample and the OP dimensionality. Starting with a set of parameters randomly generated within bounds that we specify—these include the sample geometry, density, and the six elastic moduli—we solve the elastic wave equation to produce the first N resonance frequencies that would be measured in an RUS experiment. Then using a second set of assumptions—whether the OP has one-component or two, whether our simulated experiment has k missing resonances, and the relative sizes of the elastic constant jumps produced at T_{HO} —we calculate the jumps at T_{HO} for the first n resonances (see Fig. 3). By varying the input assumptions we produce a large number of training data sets that are intended to encompass the (unknown) experimental parameters.

While the sample geometry, density, and moduli are well determined for S1 and only varied by a few tens of percent, the dimensionality of the OP, the number of missing resonances, and the sizes of the jumps in each symmetry channel are taken to be completely unknown. We vary these latter parameters across a broad range of physically possible values (see Fig. 3 and SI for further details). To prepare the simulated data for interpretation by our ANN we take the first n jumps, sort the jumps by size, normalize the jumps to lie between zero and one, and label the data sets by the dimensionality of the OP that was used to create them—either one-component or two.

This normalized and sorted list of numbers $\{\Delta f_i/f_i\}$ is used as input to an ANN. Our ANN architecture is a fully connected, feed forward neural network with a single hidden layer containing 20 neurons (see Fig. 3). Each neuron j processes the inputs $\{\Delta f_i/f_i\}$ according to the weight matrix w_{ji} and the bias vector b_j specific to that neuron as $\sigma(w_{ji}x_i + b_j)$ where the rectified linear activation function is given by $\sigma(y) \equiv \max(y, 0)$. The sum of the neural outputs is normalized via a softmax layer.

We train the ANN using 10000 sets of simulated RUS data for the case of a one-component

OP, with varied elastic constants, sample geometries, jump magnitudes, and missing resonances, and another 10000 sets for the case of a two-component OP. We use cross-entropy as the cost function for stochastic gradient descent. We train 10 different neural networks in this way to an accuracy of $\sim 90\%$, and then fix each individual network’s weights and biases. Once the networks are trained we ask each ANN for its judgment on the OP dimensionality associated with an experimentally determined set of 29 jumps, and average the responses from each neural network. The sizes of the jumps depend on how T_{HO} is assigned—assigning T_{HO} artificially far from the actual phase transition will produce large jumps in all resonances. We therefore repeat our ANN determination using a range of T_{HO} around the phase transition, and plot the outcome as a function of T_{HO} .

Fig. 4a shows the results of our ANN analysis for sample S1—the same sample discussed above using the traditional analysis. To visually compare the training and experimental data in a transparent fashion, we plot the list of sorted and normalized jumps against their indices in the list. The average of the one-component training data is shown in red; the average of the two-component training data is shown in blue; the experimental jumps are shown in grey. It is clear that the experimental data resembles the one-component training data much more closely. This resemblance is quantified in the inset, showing the ANN confidence that the experimental data belongs to the one-component class for varying assignments of T_{HO} . We find that the confidence of a one-component OP is maximized in the region of assigned T_{HO} that corresponds to the experimental value of T_{HO} .

Thus far we have shown that both methods—the traditional method of extracting the elastic moduli using the elastic wave equation, and our new method of examining the resonance spectrum directly using a trained ANN—agree that the HO parameter of URu_2Si_2 is one-component. We can now use the neural network to analyze a smaller, irregular-shaped but higher quality (higher T_{HO} (45)) sample that cannot be analyzed using the traditional method due to its

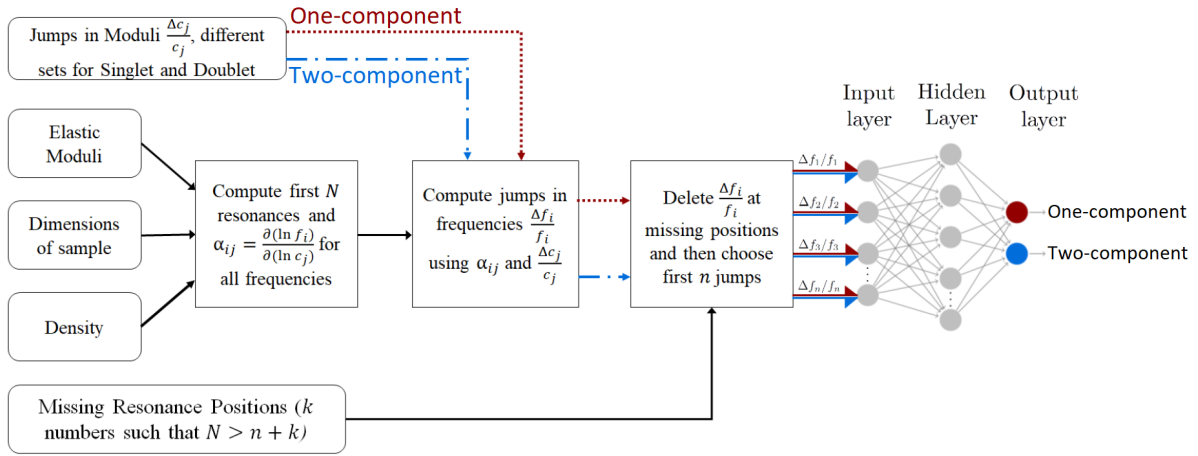


Figure 3: **Schematic of the algorithm used to generate the training data.** Values for elastic moduli and dimensions are chosen randomly from a range that bounds our experimental uncertainties. One-component OPs give jumps only in A_{1g} moduli, whereas two-component OPs also give jumps in B_{1g} and B_{2g} moduli. Separate output files are generated corresponding to one-component and two-component OPs, each containing n jumps, where n is the number of frequencies whose temperature evolution could be experimentally measured. We use scaled RUS frequency shifts $\Delta f_j / f_j$ as input to the ANN. The neurons in the hidden layer have weights w_{ij} and biases b_i . Each output neuron corresponds to one of the two OP dimensionalities under consideration, i.e. one-component and two-component. The output value of each neuron is the network's judgment on the likelihood of that OP dimensionality.

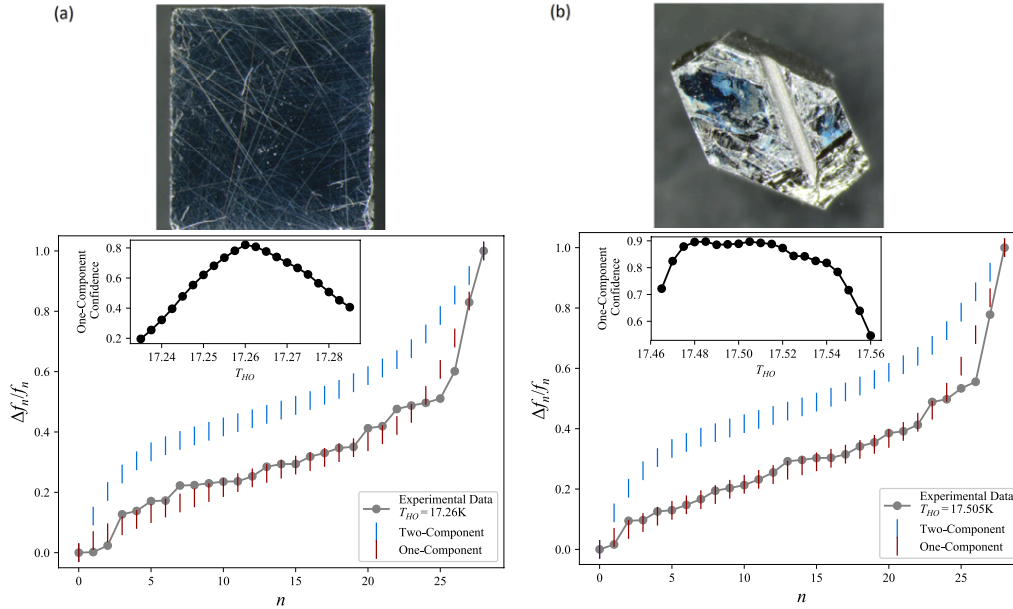


Figure 4: **Results of the ANN analysis for two samples of URu_2Si_2 .** Upper blue curves show the averaged, sorted, simulated frequency shift (“jump”) data plotted against its index in the sorted list for a two-component OP for (a) sample S1 and (b) sample S2. The data are normalized to range from 0 to 1. Lower, red curves shows the same for a one-component OP. Grey dots show experimental data for critical temperature assignment (a) $T_{\text{HO}} = 17.26$ K and (b) $T_{\text{HO}} = 17.505$ K, which visually aligns more closely with the average one-component simulated data than the two-component simulations. Insets: percent confidence of the one-component output neuron for various assignments of T_{HO} averaged over 10 trained networks. A maximum confidence of (a) 83.2% occurs for $T_{\text{HO}} = 17.26$ K and (b) 89.7% for $T_{\text{HO}} = 17.505$ K. Sample S2 has a higher value of T_{HO} due to its lower impurity concentration, as verified independently by the resistivity. Photo credits: Sayak Ghosh, Cornell University.

complicated geometry. Figure 4b shows the result of ANN analysis performed on a resonance spectrum of sample S2. The sorted and normalized spectrum looks very similar to that of S1, and the averaged ANN outcome gives 90% confidence that the OP is one-component. Despite the fact that S2 has a geometry such that the elastic moduli cannot be extracted, its resonance spectrum still contains information about the OP dimensionality and our ANN identifies this successfully.

Discussion

Our two analyses of ultrasonic resonances across T_{HO} in URu_2Si_2 strongly support one-component OPs, such as electric-hexadecapolar order (14), the chiral density wave observed by Raman spectroscopy (17, 18, 47), and are consistent with the lack of C_4 symmetry breaking observed in recent X-ray scattering experiments (30). Our analysis rules against two-component OPs, such as rank-5 superspin (19, 22) and spin-nematic order (24). The power of our result lies in its independence from the microscopic origin of the OP: group-theoretical arguments alone are sufficient to rule out large numbers of possible OPs. It could be argued that the coupling constants governing the jumps in the shear moduli are sufficiently small such that the jumps are below our experimental resolution. Previous experiments, however, have shown these coupling constants to be of the same order of magnitude in other materials with multi-component OPs (37, 48, 49). It has also been demonstrated that the size of the jump in heat capacity at T_{HO} is largely insensitive to RRR (45, 50, 51). It is therefore hard to imagine that higher RRR samples would yield jumps in the shear moduli.

The use of ANNs to analyze RUS data represents an exciting opportunity to re-examine ultrasound experiments that were previously unable to identify order parameter symmetry. For example, irregular sample geometry prevented identification of the order parameter symmetry in the high- T_c superconductor $\text{YBa}_2\text{Cu}_3\text{O}_{6.98}$ (36). Re-analysis of this spectrum using our ANN

could reveal whether the OP of the pseudogap is associated with E_u -symmetry orbital loop currents. The proposed two-component $p_x + ip_y$ superconducting state of Sr_2RuO_4 and other potential spin-triplet superconductors could also be identified in this fashion, where traditional pulse-echo ultrasound measurements have been confounded by systematic uncertainty (52).

Beyond RUS, there are many other data analysis problems in experimental physics that stand to be improved using an approach similar to the one presented here (53). In particular, any technique where simulation of a data set is straightforward but where fitting is difficult should be amenable to a framework of the type used here. The most immediately obvious technique where our algorithm could be applied is NMR spectroscopy. NMR produces spectra in a similar frequency range to RUS, but which originate in the spin-resonances of nuclear magnetic moments. Modern broad-band NMR can produce complex temperature-dependent spectra, containing resonances from multiple elements situated at different sites within the unit cell. Given a particular magnetic order it is relatively straightforward to calculate the NMR spectrum—i.e. to produce training data. The inverse problem, however, is more challenging: recovering a temperature-dependent magnetic structure from an NMR data set. In a way similar to RUS, missing resonances, and resonances mistakenly attributed to different elements, can render an analysis entirely invalid. It should be relatively straightforward to adapt our framework for generating training data and our ANN to extract temperature (or magnetic field) dependent magnetic structures from NMR spectra.

Acknowledgements

We thank P. Coleman, P. Chandra, and R. Flint for helpful discussions.

Funding

Work at Los Alamos National Laboratory was performed under the auspices of the US Department of Energy, Office of Basic Energy Sciences, Division of Materials Sciences and Engineering. M.M., B.J.R., and S.G. acknowledges support by the Cornell Center for Materials Research with funding from the NSF MRSEC program (DMR-1719875). M.M. acknowledges support by the National Science Foundation (Platform for the Accelerated Realization, Analysis, and Discovery of Interface Materials (PARADIM)) under Cooperative Agreement No. DMR-1539918. E.-A.K. acknowledge support from DOE DE-SC0018946. B.J.R. and S.G. Acknowledge funding from the National Science Foundation under Grant No. DMR-1752784.

Author Contributions

S.G. and B.J.R designed the experiment; R.B., E.D.B. grew sample S2; J.A.M. grew sample S1; S.G. acquired and analyzed the data; M.M. and E.A.K. designed the ANN; and K.A.M., A.S., M.M., S.G., and B.J.R. wrote the manuscript with input from all co-authors.

Data Availability

All data needed to evaluate the conclusions in the paper are present in the paper and/or the Supplementary Materials. Additional data available from authors upon request.

Materials and Methods

Sample S1 was grown by the Czochralski method. A single crystal oriented along the crystallographic axes was polished to dimensions $3.0\text{mm} \times 2.8\text{mm} \times 2.6\text{mm}$, with 2.6mm along the tetragonal long axis. Sample S2 was grown was grown by the Czochralski method and then processed by solid-state electrorefinement. Typical RRR values for ab-plane flakes of URu_2Si_2

taken from the larger piece range from 100-500. The RRR values measured on larger pieces (Fig. 4) are between 10-20. For a comparison of different growth methods for URu₂Si₂ see Gallagher et al. (51).

Resonant ultrasound experiments were performed in a custom-built setup consisting of two compressional-mode lithium niobate transducers, which were vibrationally isolated from rest of the apparatus. The top transducer was mounted on a freely pivoting arm, ensuring weak coupling and linear response. The response voltage generated on the pickup transducer—maximum whenever the drive frequency coincides with a sample resonance—was measured with lock-in technique. The response signal is preamplified using a custom-made charge amplifier to compensate for signal degradation in coaxial cables (54). Oxford Instruments He⁴ cryostat was used for providing temperature control.

Supplementary Information

Phase-locked Loop

Training data for ANN

Symmetry and Coupling

Lack of c_{33} jump

Resolving the origin of jumps

Compositions of Resonances

Resistance Measurement

Possible Effects from Parasitic AFM

Table S1. Calculated discontinuities (“jumps”) in elastic moduli for one- and two-component order parameters in a tetragonal system.

Fig. S1. Resonant ultrasound using phase-locked loop.

Fig. S2. Three representative resonance frequencies of URu₂Si₂ and their attenuation through

T_{HO} .

Fig. S3. Elastic moduli of URu_2Si_2 with the contribution above T_{HO} subtracted.

Fig. S4. Fitting temperature evolution of resonances.

Fig. S5. Resistance of sample S2 measured from 300K down to 2K.

Competing Interests

The authors declare that they have no competing interests.

References

1. J. A. Mydosh, P. M. Oppeneer, *Rev. Mod. Phys.* **83**, 1301 (2011).
2. J. Mydosh, P. Oppeneer, *Philosophical Magazine* **94**, 3642 (2014).
3. B. J. Ramshaw, *et al.*, *Proceedings of the National Academy of Sciences* **112**, 3285 (2015).
4. J. Carrasquilla, R. G. Melko, *Nature Physics* **13**, 431 EP (2017).
5. R. Ouyang, S. Curtarolo, E. Ahmetcik, M. Scheffler, L. M. Ghiringhelli, *Phys. Rev. Materials* **2**, 083802 (2018).
6. A. Bohrdt, *et al.*, *Nature Physics* **15**, 921 (2019).
7. B. S. Rem, *et al.*, *Nature Physics* **15**, 917 (2019).
8. Y. Zhang, *et al.*, *Nature* **570**, 484 (2019).
9. Y. Yamaji, T. Yoshida, A. Fujimori, M. Imada, Hidden self-energies as origin of cuprate superconductivity revealed by machine learning (2019).

10. H. Harima, K. Miyake, J. Flouquet, *Journal of the Physical Society of Japan* **79**, 033705 (2010).
11. F. J. Ohkawa, H. Shimizu, *Journal of Physics: Condensed Matter* **11**, L519 (1999).
12. P. Santini, G. Amoretti, *Phys. Rev. Lett.* **73**, 1027 (1994).
13. A. Kiss, P. Fazekas, *Phys. Rev. B* **71**, 054415 (2005).
14. K. Haule, G. Kotliar, *Nature Physics* **5**, 796 EP (2009).
15. H. Kusunose, H. Harima, *Journal of the Physical Society of Japan* **80**, 084702 (2011).
16. F. Cricchio, F. Bultmark, O. Grånäs, L. Nordström, *Phys. Rev. Lett.* **103**, 107202 (2009).
17. H.-H. Kung, *et al.*, *Science* **347**, 1339 (2015).
18. H.-H. Kung, *et al.*, *Phys. Rev. Lett.* **117**, 227601 (2016).
19. S. Kambe, *et al.*, *Phys. Rev. B* **97**, 235142 (2018).
20. P. Thalmeier, T. Takimoto, *Phys. Rev. B* **83**, 165110 (2011).
21. S. Hoshino, J. Otsuki, Y. Kuramoto, *Journal of the Physical Society of Japan* **82**, 044707 (2013).
22. J. G. Rau, H.-Y. Kee, *Phys. Rev. B* **85**, 245112 (2012).
23. S. Tonegawa, *et al.*, *Phys. Rev. Lett.* **109**, 036401 (2012).
24. S. Fujimoto, *Phys. Rev. Lett.* **106**, 196407 (2011).
25. H. Ikeda, *et al.*, *Nature Physics* **8**, 528 EP (2012).
26. S. C. Riggs, *et al.*, *Nature Communications* **6**, 6425 EP (2015).

27. It is also generally agreed that OP of the HO state orders at a finite wavevector of $Q = (0, 0, 1/2)$. Because our measurement occurs close to $Q = 0$, i.e. at long wavelength, we are only concerned with the point-group symmetry of the OP, and not with its modulation in space.
28. R. Okazaki, *et al.*, *Science* **331**, 439 (2011).
29. S. Tonegawa, *et al.*, *Nature communications* **5**, 4188 (2014).
30. J. Choi, *et al.*, *Phys. Rev. B* **98**, 241113 (2018).
31. V. Aji, A. Shekhter, C. Varma, *Physical Review B* **81**, 064515 (2010).
32. T. Rice, M. Sigrist, *Journal of Physics: Condensed Matter* **7**, L643 (1995).
33. N. Read, D. Green, *Phys. Rev. B* **61**, 10267 (2000).
34. N. Harrison, M. Jaime, *arXiv preprint arXiv:1902.06588* (2019).
35. P. Chandra, P. Coleman, R. Flint, *Nature* **493**, 621 EP (2013). Article.
36. A. Shekhter, *et al.*, *Nature* **498**, 75 (2013).
37. B. Lüthi, T. J. Moran, *Phys. Rev. B* **2**, 1211 (1970).
38. T. Fukase, *et al.*, *Japanese Journal of Applied Physics* **26**, 1249 (1987).
39. G. Bullock, B. Shivaram, D. G. Hinks, *Physica C: Superconductivity* **169**, 497 (1990).
40. B. Wolf, *et al.*, *Physica B: Condensed Matter* **199**, 167 (1994).
41. T. Yanagisawa, *et al.*, *Journal of Physics: Conference Series* (IOP Publishing, 2012), vol. 391, p. 012079.

42. T. Yanagisawa, *et al.*, *Phys. Rev. B* **97**, 155137 (2018).
43. There are two A_{1g} strains, $\epsilon_{xx} + \epsilon_{yy}$ and ϵ_{zz} with associated moduli $(c_{11} + c_{12})/2$ and c_{33} , as well as linear coupling between these two strains that produces a third modulus c_{23} . To simplify the notation we drop the sum over all three of these terms in the free energy.
44. K. A. Modic, *et al.*, *Nature Communications* **9** (2018).
45. R. Baumbach, *et al.*, *Philosophical Magazine* **94**, 3663 (2014).
46. B. C. Csáji, *Faculty of Sciences, Eötvös Loránd University, Hungary* **24**, 48 (2001).
47. J. Buhot, *et al.*, *Phys. Rev. Lett.* **113**, 266405 (2014).
48. T. Ikeda, K. Fujibayashi, T. Nagai, J. Kobayashi, *physica status solidi (a)* **16**, 279 (1973).
49. C. W. Garland, J. S. Jones, *The Journal of Chemical Physics* **39**, 2874 (1963).
50. T. D. Matsuda, *et al.*, *Journal of the Physical Society of Japan* **80**, 114710 (2011).
51. A. Gallagher, *et al.*, *Crystals* **6**, 128 (2016).
52. N. Okuda, T. Suzuki, Z. Mao, Y. Maeno, T. Fujita, *Journal of the Physical Society of Japan* **71**, 1134 (2002).
53. J. Greitemann, K. Liu, L. Pollet, *Phys. Rev. B* **99**, 060404 (2019).
54. A. Migliori, J. D. Maynard, *Review of Scientific Instruments* **76**, 121301 (2005).
55. S. Altmann, P. Herzig, *Point-group theory tables* (Oxford, 1994).
56. W. Rehwald, *Advances in Physics* **22**, 721 (1973).
57. K. Miyake, C. M. Varma, *Phys. Rev. Lett.* **57**, 1627 (1986).

58. K. Matsuda, Y. Kohori, T. Kohara, K. Kuwahara, H. Amitsuka, *Phys. Rev. Lett.* **87**, 087203 (2001).
59. T. Yanagisawa, *Philosophical Magazine* **94**, 3775 (2014).

Supplementary Information

Phase-locked Loop

The traditional method to track resonance frequencies with temperature in RUS is to fit a Lorentzian to find the resonance, and this requires measuring the spectra in a small frequency range around the resonance at every temperature. For our RUS measurements, we use a phase-locked loop (PLL) to track resonance frequencies as a function of temperature, which eliminates the need to scan over a frequency range at every temperature. PLL comprises a lock-in amplifier coupled to a PID controller. Lock-in measures amplitude and phase of the response at the drive frequency, and the PID controller adjusts drive frequency so as to maintain the phase at a setpoint. We typically choose the phase setpoint to coincide with the peak of the resonance since the phase changes most rapidly there. We find that compared to traditional RUS, PLL tracks resonances with higher sensitivity and the standard error is lower by a factor of 30 (see Figure 5). As there is no need to do a frequency scan and perform a Lorentzian fit at every temperature, this is also a faster measurement yielding ~ 1000 times more points per unit temperature. To the best of our knowledge, a phase-locked loop technique has never been employed before in resonant ultrasound spectroscopy studies.

Training data for ANN

We generate simulated RUS spectra for training the artificial neural network (ANN). We first solve the 3-D elastic wave equation using input parameters—density of sample, elastic constants and dimensions—which are chosen from a range that bounds our experimental uncertainties, to obtain the first N lowest frequency resonances and their compositions ($\alpha_{ij} = \partial(\ln f_i)/\partial(\ln c_j)$) in terms of the six independent elastic constants. We expect different sets of jumps in moduli ($\Delta c_j/c_j$) for one- and two-component OPs (see ‘Symmetry and Coupling’ section for details), which translate into different sets of jumps in resonance frequencies ($\Delta f_i/f_i$) for the two OP

types. Experimentally, some resonances are too noisy to be measured through the transition, and to account for that, we delete a random number (k) of jumps from the the list of N consecutive $\Delta f_i/f_i$. We then choose the first n jumps to constitute a training data set, where n is the number of jumps measured in experiment.

Symmetry and Coupling

In a tetragonal crystal, elastic strain breaks into five irreducible representations, two compressive strains transforming as the A_{1g} representation and three shear strains transforming as the B_{1g} , B_{2g} and E_g representations [3]. The elastic free energy density is given by

$$\begin{aligned}
\mathcal{F}_{el} &= \frac{1}{2} \left(c_{11}(\epsilon_{xx}^2 + \epsilon_{yy}^2) + 2c_{12}\epsilon_{xx}\epsilon_{yy} + c_{33}\epsilon_{zz}^2 + 2c_{13}(\epsilon_{xx} + \epsilon_{yy})\epsilon_{zz} + 4c_{44}(\epsilon_{xz}^2 + \epsilon_{yz}^2) + 4c_{66}\epsilon_{xy}^2 \right) \\
&= \frac{1}{2} \left(\frac{c_{11} + c_{12}}{2}(\epsilon_{xx} + \epsilon_{yy})^2 + c_{33}\epsilon_{zz}^2 + 2c_{13}(\epsilon_{xx} + \epsilon_{yy})\epsilon_{zz} + \frac{c_{11} - c_{12}}{2}(\epsilon_{xx} - \epsilon_{yy})^2 + \right. \\
&\quad \left. 4c_{44}(\epsilon_{xz}^2 + \epsilon_{yz}^2) + 4c_{66}\epsilon_{xy}^2 \right) \\
&= \frac{1}{2} \left(c_{A_{1g},1}\epsilon_{A_{1g},1}^2 + c_{A_{1g},2}\epsilon_{A_{1g},2}^2 + 2c_{A_{1g},3}\epsilon_{A_{1g},1}\epsilon_{A_{1g},2} + c_{B_{1g}}\epsilon_{B_{1g}}^2 + c_{E_g}|\epsilon_{E_g}|^2 + c_{B_{2g}}\epsilon_{B_{2g}}^2 \right)
\end{aligned} \tag{1}$$

where the strains are written as the irreducible representations of D_{4h} , $(\epsilon_{xx} + \epsilon_{yy}) \rightarrow \epsilon_{A_{1g},1}$, $\epsilon_{zz} \rightarrow \epsilon_{A_{1g},2}$, $(\epsilon_{xx} - \epsilon_{yy}) \rightarrow \epsilon_{B_{1g}}$, $2\epsilon_{xy} \rightarrow \epsilon_{B_{2g}}$ and $(2\epsilon_{xz}, 2\epsilon_{yz}) \rightarrow \epsilon_{E_g}$.

We consider integer representations of D_{4h} in the following calculations. Half-integer representations have been addressed at the end of this section.

Following Landau theory, near a phase transition, an order parameter(OP) η is introduced whose contribution to the free energy density is

$$\mathcal{F}_0^s(\eta) = a\eta^2 + \frac{b}{2}\eta^4 \tag{2}$$

For a two-component OP (η_x, η_y) , this becomes

$$\mathcal{F}_0^d(\eta_x, \eta_y) = a(\eta_x^2 + \eta_y^2) + \frac{b_0}{4}(\eta_x^2 + \eta_y^2)^2 + \frac{b_1}{4}(\eta_x^2 - \eta_y^2)^2 + b_2\eta_x^2\eta_y^2 \tag{3}$$

with $a = a_0(T - T_{HO})$, and $a, b, b_{0,1,2} > 0$. With strain-OP coupling(\mathcal{F}_c), the total free energy density becomes

$$\mathcal{F} = \mathcal{F}_0(\eta_i) + \mathcal{F}_{el}(\epsilon_\mu) + \mathcal{F}_c(\eta_i, \epsilon_\mu) \quad (4)$$

The coupling between OP and various symmetry strains leads to the corresponding elastic constants getting modified in the ordered state. Since the free energy density must transform like the identity A_{1g} representation, only those couplings are allowed in \mathcal{F}_c which transform as A_{1g} under symmetry operations of the tetragonal(D_{4h}) group.

The square of any one-component order parameter has A_{1g} symmetry, and hence an one-component OP can couple to only A_{1g} strains. A two-component OP in a tetragonal crystal belongs to $E_{g/u}$ representation and since the square of an $E_{g/u}$ object has A_{1g} , B_{1g} and B_{2g} symmetry objects, we expect a two-component OP to couple to $\epsilon_{B_{1g}}$ and $\epsilon_{B_{2g}}$ in addition to the two A_{1g} strains. None of the OPs can couple to ϵ_{E_g} .

Written explicitly, the coupling free energy reads

$$\mathcal{F}_c^s = (g_1\epsilon_{A_{1g,1}} + g_2\epsilon_{A_{1g,2}})\eta^2 \quad (5)$$

for one-component OPs and

$$\mathcal{F}_c^d = (g_1\epsilon_{A_{1g,1}} + g_2\epsilon_{A_{1g,2}})(\eta_x^2 + \eta_y^2) + g_4\epsilon_{B_{1g}}(\eta_x^2 - \eta_y^2) + \frac{g_5}{2}\epsilon_{B_{2g}}\eta_x\eta_y \quad (6)$$

for two-component OPs in a tetragonal system. Clearly, for non-zero discontinuity(“jump”) in a particular moduli c_μ , there needs to be an allowed coupling term between the associated symmetry strain ϵ_μ and the order parameter.

As a concrete example, we consider a two-component OP (η_x, η_y) of E -symmetry and calculate jumps in the various moduli. Minimizing \mathcal{F}_0^d gives two distinct equilibrium OPs depending on the relative magnitudes of b_1 and b_2 .

$$(\eta_x^0, \eta_y^0) = \begin{cases} \sqrt{-\frac{2a}{b_0+b_1}}\{(\pm 1, 0), (0, \pm 1)\} & , b_1 < b_2 \\ \sqrt{-\frac{a}{b_0+b_2}}(\pm 1, \pm 1) & , b_1 > b_2 \end{cases} \quad (7)$$

Dimensionality	Symmetry	$\Delta c_{A_{1g},1}$	$\Delta c_{A_{1g},2}$	$\Delta c_{A_{1g},3}$	$\Delta c_{B_{1g}}$	$\Delta c_{B_{2g}}$
One-component	A_1, A_2, B_1, B_2	$\frac{-g_1^2}{b}$	$\frac{-g_2^2}{b}$	$\frac{-g_1 g_2}{b}$	0	0
Two-component	$E(\pm 1, 0), E(0, \pm 1)$	$\frac{-2g_1^2}{(b_0+b_1)}$	$\frac{-2g_2^2}{(b_0+b_1)}$	$\frac{-2g_1 g_2}{(b_0+b_1)}$	$\frac{-2g_4^2}{(b_0+b_1)}$	$\frac{-2g_5^2}{(b_2-b_1)}$
	$E(\pm 1, \pm 1)$	$\frac{-2g_1^2}{(b_0+b_2)}$	$\frac{-2g_2^2}{(b_0+b_2)}$	$\frac{-2g_1 g_2}{(b_0+b_2)}$	$\frac{-2g_4^2}{(b_1-b_2)}$	$\frac{-2g_5^2}{(b_0+b_2)}$

Table 2: Calculated discontinuities (“jumps”) in elastic moduli for one- and two-component order parameters in a tetragonal system.

For $b_1 < b_2$, the 4 possible states(all of which are physically equivalent) are denoted as $E(\pm 1, 0)$ for $\eta_y^0 = 0$ and $E(0, \pm 1)$ for $\eta_x^0 = 0$. For $b_1 > b_2$, the possible equivalent states are denoted as $E(\pm 1, \pm 1)$. To calculate strain-dependent corrections to the equilibrium OP (η_x^0, η_y^0) , we perturb $(\eta_x^0, \eta_y^0) \rightarrow (\eta_x^0 + \tilde{\eta}_x, \eta_y^0 + \tilde{\eta}_y)$ and expand the (η_x, η_y) -dependent terms in \mathcal{F} up to quadratic order in $(\tilde{\eta}_x, \tilde{\eta}_y)$. Minimizing with respect to $\tilde{\eta}_x$ and $\tilde{\eta}_y$ then reduces to solving two linear equations, which give us the modified OP. Finally, replacing this OP in \mathcal{F} and taking appropriate strain derivatives allows to straightforwardly calculate the modified elastic constants in the ordered state.

The calculated jumps in the various moduli for all the integer representation OPs of D_{4h} are tabulated in Supplementary Table 2. Clearly, a two-component OP induces jumps in both of the in-plane shear(B_{1g} and B_{2g}) moduli in addition to the compressional(A_{1g}) moduli, while an one-component OP only modifies the A_{1g} moduli, as expected. This leads to different sets of $\Delta c_j/c_j$ for one-component and two-component OPs, which we use to generate training data for the neural network (detailed in Figure 3 of the main text and the ‘Training data for ANN’ section). We note that the non-zero shear jumps concluded from our calculations refute the claim made in [20] that shear moduli are continuous through the hidden order transition.

D_{4h} also contains half-integer representations, such as $E_{3/2,g}$ which is the representation of the slave boson responsible for the “hastatic” order parameter proposed by Chandra *et al.*

[35] ($E_{3/2,g}$ is also known as Γ_7^+). $E_{3/2,g}$ forms bilinears of the A_{2g} and E_g representations (see Altmann and Herzig [55] table 33.8): this predicts no jump in either c_{66} or $(c_{11} - c_{12})/2$, but does predict a jump in c_{44} , which we also do not observe. If, however, the hastatic order only forms bilinears at finite \mathbf{q} , then it will predict no jumps in any of the elastic moduli.

Lack of c_{33} jump

In our experiment, we do not see a discontinuity in c_{33} elastic constant, although it is expected for an one-component OP. From Supplementary Table 2, the three A_{1g} jumps can be related as

$$\Delta c_{A_{1g},1} \times \Delta c_{A_{1g},2} = (\Delta c_{A_{1g},3})^2 \quad (8)$$

Experimentally we measure relative jumps ($\frac{\Delta c}{c}$), which can be related by rewriting Equation 8 as

$$\begin{aligned} \frac{\Delta c_{A_{1g},2}}{c_{A_{1g},2}} \cdot c_{A_{1g},2} &= \frac{\left(\frac{\Delta c_{A_{1g},3}}{c_{A_{1g},3}} \cdot c_{A_{1g},3}\right)^2}{\left(\frac{\Delta c_{A_{1g},1}}{c_{A_{1g},1}} \cdot c_{A_{1g},1}\right)} \\ \implies \left(\frac{\Delta c_{A_{1g},2}}{c_{A_{1g},2}}\right) &= \frac{1}{c_{A_{1g},2}} \cdot \frac{\left(\frac{\Delta c_{A_{1g},3}}{c_{A_{1g},3}} \cdot c_{A_{1g},3}\right)^2}{\left(\frac{\Delta c_{A_{1g},1}}{c_{A_{1g},1}} \cdot c_{A_{1g},1}\right)} \end{aligned} \quad (9)$$

Using the known jumps in $(c_{11} + c_{12})/2$ and c_{23} (see Figure 2 of the main text and Equation 1), we estimate $\frac{\Delta c_{33}}{c_{33}} \approx 4 \times 10^{-7}$, which is an order of magnitude below our experimental resolution. This explains the lack of c_{33} jump in our experimental data.

Resolving the Origin of Jumps

The elastic moduli discontinuities predicted by $g\eta^2\epsilon$ coupling in Landau theory only show up in experiments under the assumption that the applied strain varies at a timescale much longer than the relaxation times of the order parameter [56]. Our experiments are in the low MHz frequency range, corresponding to timescales of order 10^{-7} s. The HO transition is a mean-field like second order transition, and the OP relaxation timescales for similar (superconducting)

transitions in other uranium-based heavy fermion compounds are of the order $10^{-10} - 10^{-12}$ s [57]. Thus our experimental frequencies are low enough to observe the moduli jumps.

To rule out anomalous OP dynamics near the phase transition interfering with our measured jumps, we look at the ultrasonic attenuation in the resonances through T_{HO} . In particular, anomalous OP dynamics would lead to large, temperature-dependent features in the attenuation near T_{HO} . In Figure 6, we plot the temperature evolution of three resonances, each showing a clear discontinuity at T_{HO} . The inverse quality factor of these frequencies (proportional to ultrasonic attenuation), plotted in panel (d), show tiny features at T_{HO} , but overall unremarkable behavior. The tiny features are required by Kramers-Kronig relations, but the overall behavior is dominated by phonon anharmonicity and not OP dynamics. Our plot (see Figure 7) of the elastic moduli with the background contribution subtracted further highlights the singular nature of the discontinuity in the A_{1g} moduli.

This confirms that the moduli jumps we see originate from strain-order parameter coupling terms of the form $g\eta^2\epsilon$, and hence our measured jumps constrain the order parameter in URu_2Si_2 to be one-component.

Compositions of Resonances

The irregular shape of the higher quality sample S2 prevents directly inverting the frequency spectra to calculate the elastic moduli and the compositions of the frequencies in terms of the moduli (α_{ij} s). To estimate the compositions, we use the known temperature evolution of the 6 elastic constants between 145K to 25K to fit the change in frequencies as the sample is cooled in this temperature range (Figure 8). This helps us ensure that the sample S2 has in-plane shear (B_{1g} and B_{2g}) modes in our experimentally accessible frequency range, and hence the data we obtain should allow us to distinguish between one- and two-component order parameters.

Resistance Measurement

We checked the quality of sample S2 by measuring its resistance from 300K down to 2K, as shown in Figure 9. The Kondo crossover is seen around $T^* = 75\text{K}$ and the resistance shows a sudden increase at the HO transition, consistent with previous reports. We use the feature near the hidden order transition to determine $T_{HO} = 17.52\text{K}$ for this sample. This value of T_{HO} [45,51] confirms the higher quality of S2 compared to S1.

Possible Effects from Parasitic AFM

Under hydrostatic pressure, URu_2Si_2 undergoes a transition into a large moment antiferromagnet (LMAF) phase. Even at ambient pressure, URu_2Si_2 samples are known to host some amount of this parasitic AFM phase, arising from inhomogeneous strain in the sample [58]. The AFM phase shows a large discontinuity in the modulus c_{11} [59]. One could imagine that the jumps we see at T_{HO} are arising from the presence of this parasitic AFM phase, in particular for sample S1, since it has a suppressed $T_{HO} = 17.25\text{ K}$, compared to the standard $T_{HO} = 17.5\text{ K}$.

To confirm that we are seeing discontinuities from the HO phase, we obtained the high-purity sample S2, which underwent solid-state electrorefinement, and has $T_{HO} = 17.5\text{ K}$. It can be seen that sample S2 shows the same distribution of jumps as S1 (see Figure 4 of the main text). This rules against any parasitic effects leading to the jumps, since these samples must have very different concentrations of AFM puddles in them. Additionally, we note that the elastic anomalies due to strain-induced AFM should appear at T_N , which is a different temperature than T_{HO} . We see only a single transition, as evidenced by a single jump in A_{1g} moduli and a change in slope in the shear moduli, all happening at the HO transition temperature (as defined by resistance measurements shown in Figure 9). If the elastic anomalies were to arise from strain-induced AFM, we would expect these signatures of the phase transition to show up at a different temperature than exactly T_{HO} (or more likely, a distribution of temperatures, since

the strain relaxes over a finite lengthscale away from the parasitic regions). We resolve a sharp (~ 100 mK) transition, and hence if there were two transitions, we should be able to see them.

The fact that our results are consistent between sample S1 and S2, and we see only a single sharp transition at precisely T_{HO} , confirms that the elastic discontinuities are from the HO transition, and not due to strain-induced AFM.

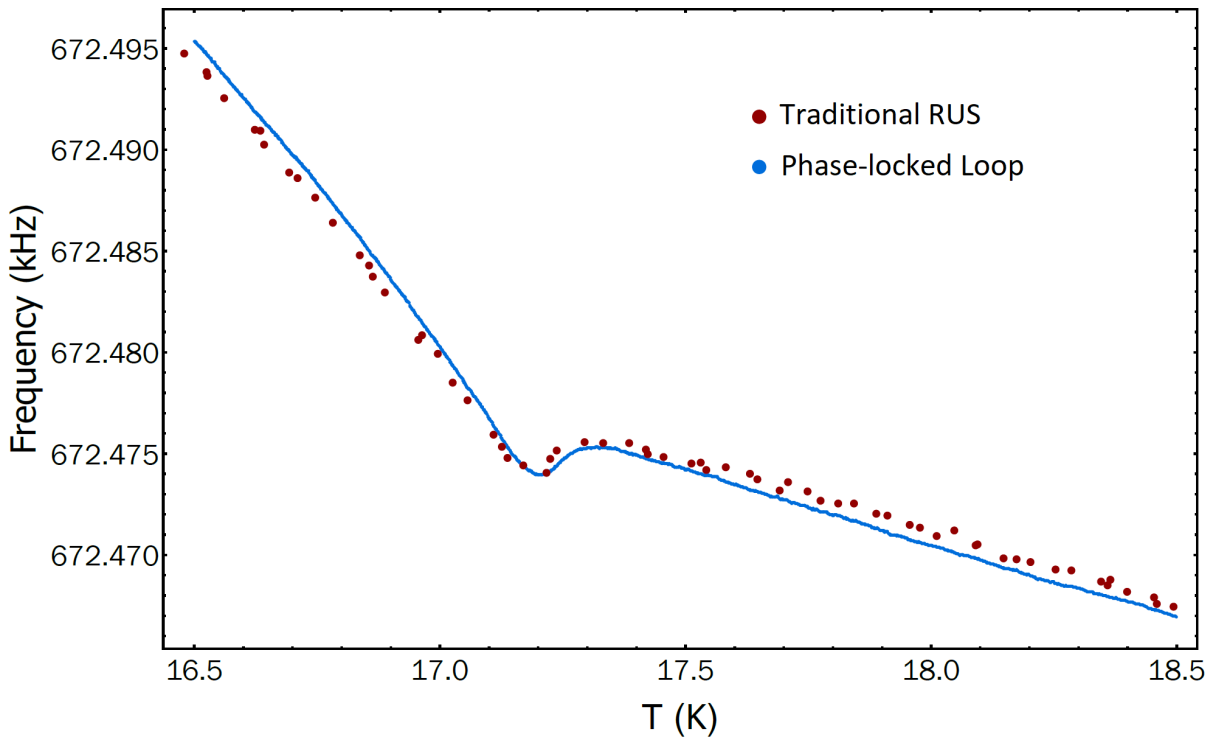


Figure 5: Resonant ultrasound using phase-locked loop. We compare data between fitting Lorentzian(traditional RUS) and phase-locked loop(PLL) for the same resonance frequency as sample is cooled through the hidden order transition. Data taken with PLL has lower fluctuations and a much higher density of frequency points.

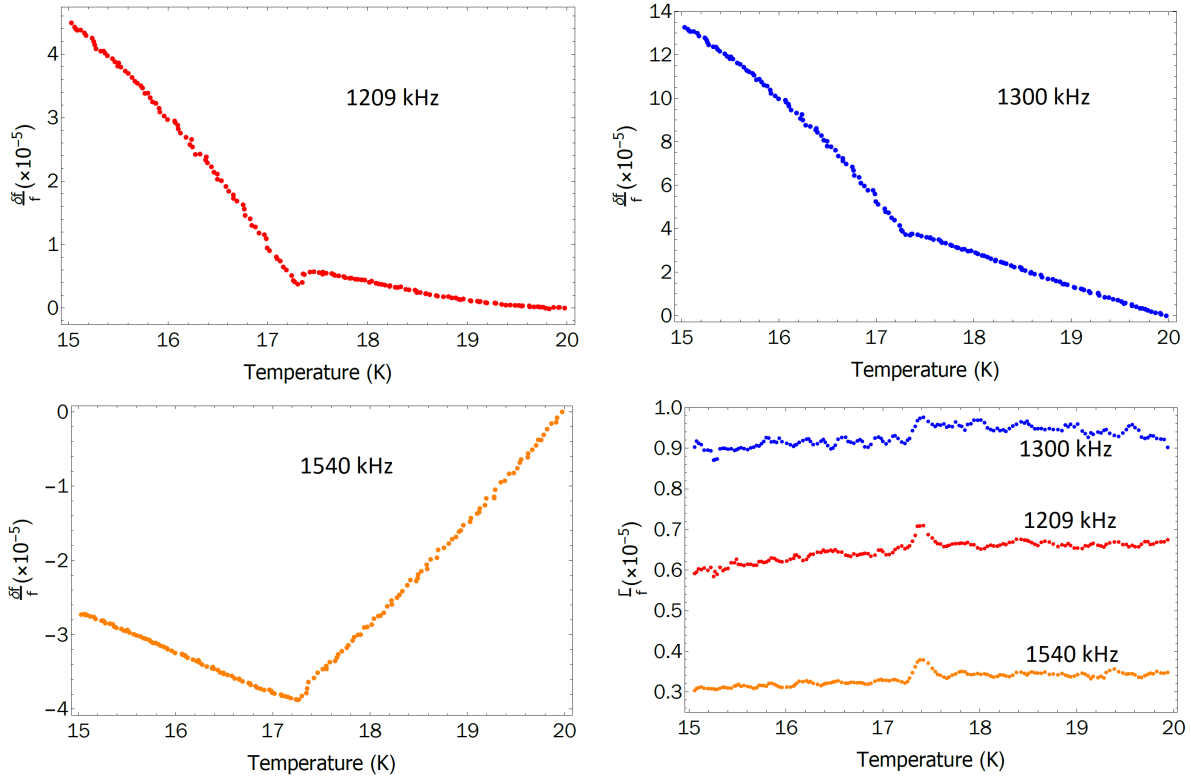


Figure 6: Three representative resonance frequencies of URu_2Si_2 and their attenuation through T_{HO} . A clear discontinuity can be seen in all three resonances and a small peak-like feature can be seen in the attenuation at T_{HO} . The lack of any large temperature-dependent feature in the attenuation rules out anomalous order parameter dynamics interfering with our results.

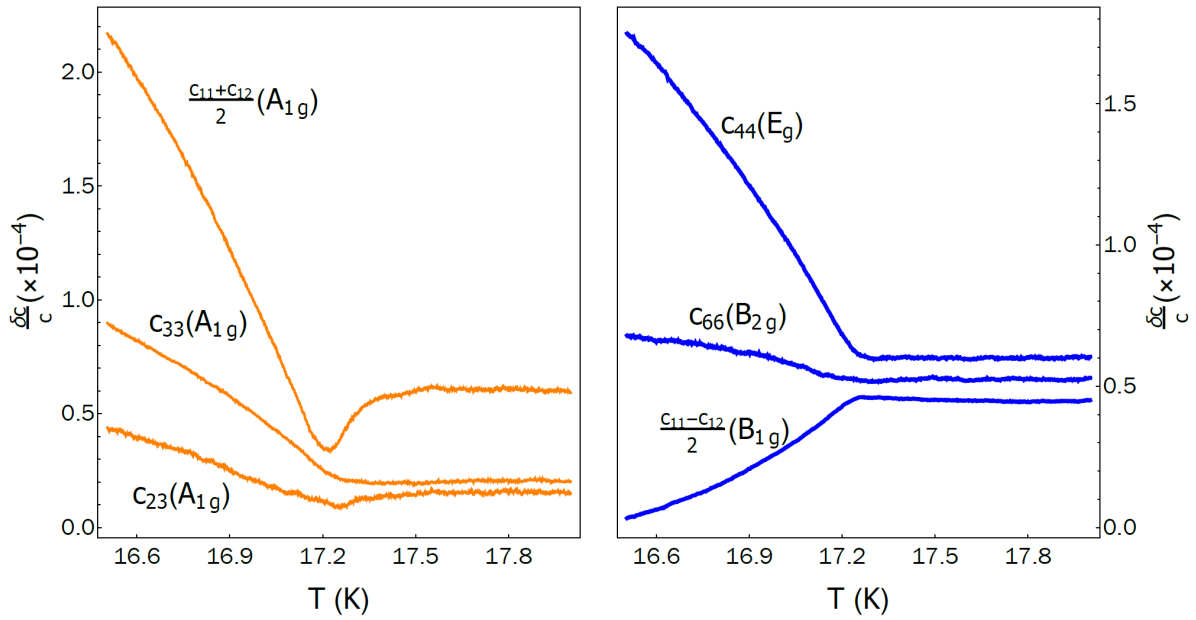


Figure 7: Elastic moduli of URu_2Si_2 with the contribution above T_{HO} subtracted. This procedure isolates the effect of the order parameter on the moduli. Plots are vertically shifted for visual clarity. It can be clearly seen that $(c_{11} + c_{12})/2$ and c_{23} show a drop at T_{HO} before starting to stiffen in the HO phase, while all other moduli only show increased stiffening/softening through T_{HO} .

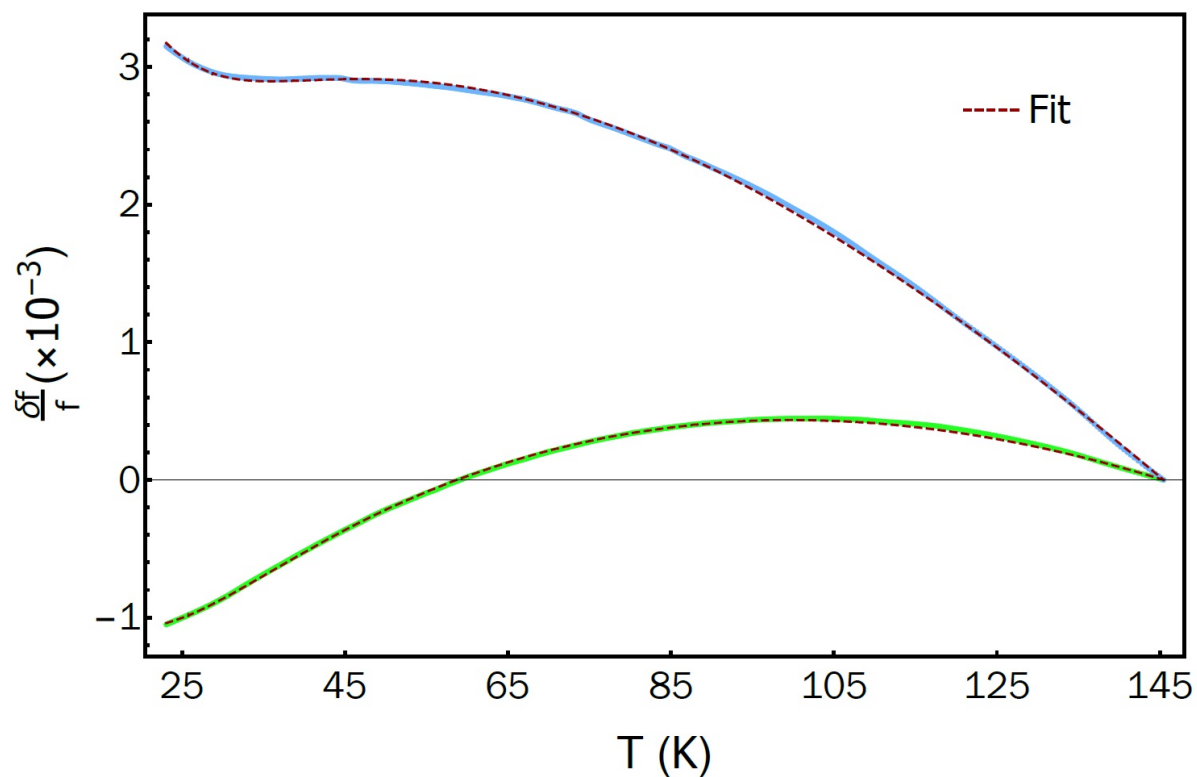


Figure 8: Fitting temperature evolution of resonances. Temperature dependence of two representative resonances (blue and green) between $\sim 25\text{K}$ to 145K . The fit estimates that the blue curve is composed of mostly E_g and some A_{1g} symmetry vibrations, whereas the green curve is dominated by vibrations in B_{1g} channel.

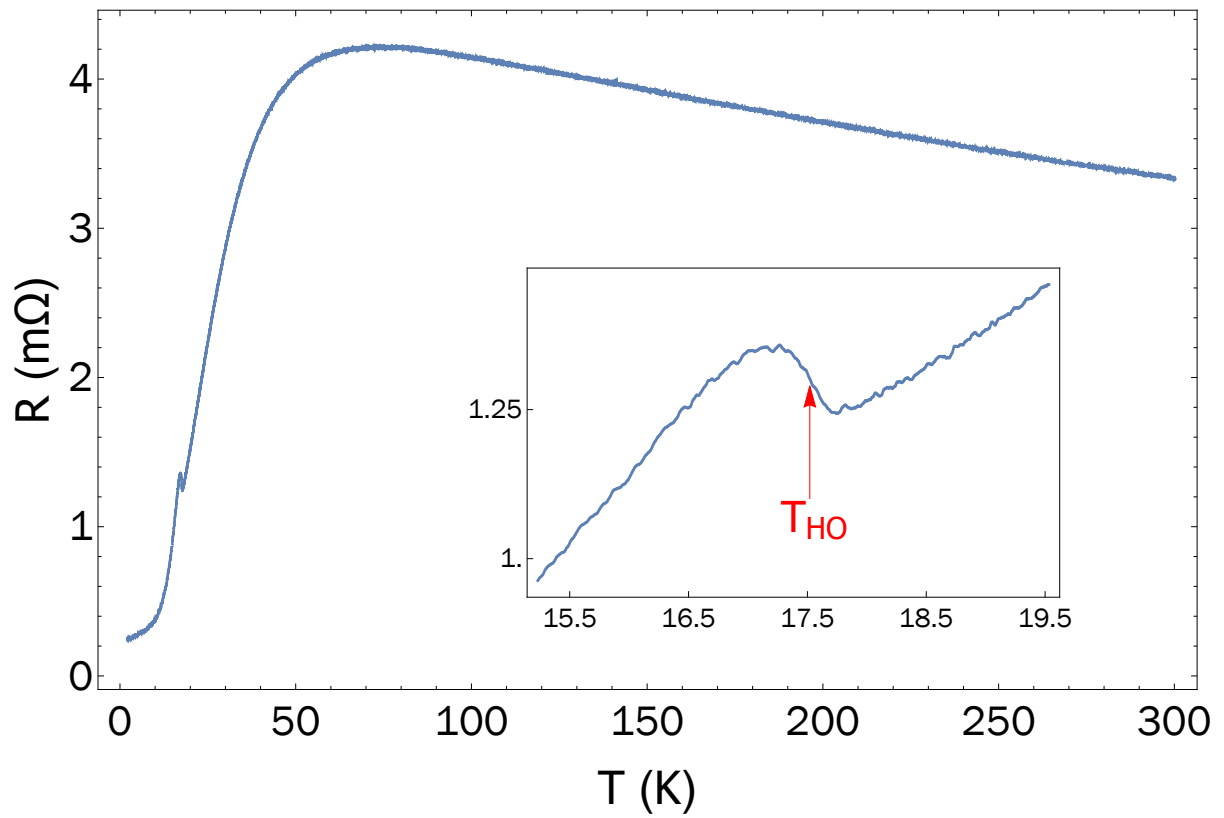


Figure 9: Resistance of sample S2 measured from 300K down to 2K. Inset shows the feature at hidden order transition, from which we determine $T_{HO} = 17.52K$ for this sample.